Design and Calibration of a Double-directional 60 GHz Channel Sounder for Multipath Component Tracking*

Ruoyu Sun[1], Peter B. Papazian[1], Jelena Senic[1], Yeh Lo[1], Jae-Kark Choi[2], Kate A. Remley[1], Camillo Gentile[2]

[1]RF Technology Division, National Institute of Standards and Technology, Boulder, CO, USA, ruoyu.sun@nist.gov
[2]Wireless Networks Division, National Institute of Standards and Technology, Gaithersburg, MD, USA

***Abstract*—The 60 GHz band is being considered for many high-bandwidth wireless applications. To support standards development for these applications, NIST has developed an untethered 60 GHz, 8×16 MIMO channel sounder. It employs a pseudorandom bit sequence with a bandwidth of 4 GHz. The sounder can precisely measure radio propagation channel characteristics such as path loss, small-scale fading, delay dispersion, absolute delay, angle-of-arrival (AoA), angle-of-departure (AoD), and Doppler power spectrum. Its ability to measure the time dynamics of the millimeter-wave radio channel, when untethered and in motion, is unique. It employs electronically-switched MIMO antenna arrays, a robot for moving measurements and an automated one-dimensional positioner for precision measurements at fixed locations. Sounder performance is improved by use of pre-distortion filters and precision calibration of the RF and timing systems. Data showing initial AoD and AoA estimation error are presented along with initial test results for ground-plane reflection.**

***Index Terms*—mmWave, MIMO, channel; measurement.**

I. INTRODUCTION

In July 2016, the Federal Communications Commission (FCC) granted approval of licensed operation in new 28, 37, and 39 GHz bands and extended the unlicensed 60 GHz band from 57 – 71 GHz, releasing in total about 11 GHz of millimeter-wave (mmWave) spectrum [1]. The band at 95 GHz is also currently under review. The order was prompted by the saturation of the sub-6 GHz allocations over the past decade, in particular by data-intensive smartphones. Although less favorable in terms of propagation, the new bands will admit channel bandwidths three orders of magnitude wider; indeed, the IEEE 802.11ay standardization efforts in process have already provisioned for 4.4 GHz channels to support use cases including outdoor backhaul, wireless server backup, augmented reality headsets, and mass video distribution [1].

More than a simple shift in center frequency, mmWave communication systems embody a significant departure in technology from their predecessors. The tiny wavelengths relax the conditions for implementing phased-array antennas with tens to hundreds of elements on a mobile handset (as well as at the base station). The massive arrays can synthesize extremely narrow beams on the order of degrees. The purpose is, through their associated gain in excess of 30 dBi, to compensate for the greater path loss witnessed in the upper spectrum. In order for beamforming to take full advantage of the propagation environment, channel sounding will allow a base station and user device to jointly determine which angles-of-departure (AoDs) and angles-of-arrival (AoAs) correspond to viable transmission paths. The beams will then be steered in those multipath directions. Frequent updating of the channel state through multipath component tracking will be necessary in mobile environments to avoid the beams falling out of alignment with the multipaths. Hence multipath tracking represents a novel but critical aspect of mmWave channel propagation modeling.

To help meet the demands of these next-generation models, NIST has designed the 60 GHz channel sounder described in this paper. The three-dimensional antenna arrays at the transmitter (TX) and receiver (RX) permit extraction of double-directional multipath components in both azimuth and elevation. By virtue of the electronically-switched arrays, a complete channel measurement can be realized in just 262 µs. Combined with the untethered design enabled by synchronization through rubidium clocks, mobile environments up to a closing speed of 35 km/h can be characterized. Finally, the 4 GHz null-to-null bandwidth of the system can accommodate the use cases anticipated for mmWave systems.

II. SYSTEM DESIGN

A. Overview

The 60 GHz sounder system has design features which are similar to the 83 GHz sounder described in [2]-[4]. As with the E-band system, it utilizes a pseudorandom bit sequence (PRBS) to measure the complex channel impulse response (CIR), a 16-element antenna array with fast switching multiplexer (MUX) at the receiver, and a mobile positioner to provide position information and mapping. In contrast to the single transmit antenna, this 60 GHz system has an 8-element switched array. Thus, the MIMO capability allows measurement of AoD as well as AoA. Both antenna arrays use scalar feed horns (SFHs) which have symmetrical patterns, maximum gain of 18.1 dBi and side-lobe levels below -10 dBi. This is important when combining patterns in an array processing program and making use of the space-alternating generalized expectation-maximization (SAGE) algorithm [5] to calculate the equivalent omni-directional CIRs. In addition to its mobile measurement capabilities, a one-dimensional (1-D) positioner has been added for stationary measurements at sub-wavelength increments. The system parameters as well as additional calibration methods are discussed in the following sections.

B. Transmitter and Receiver

The TX utilizes an arbitrary waveform generator (AWG) with a sampling rate of 12 Gsamples/s. The AWG generates a

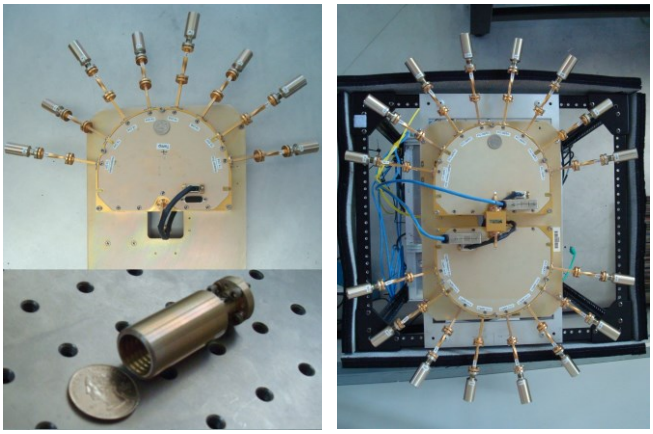

Fig. 1. Photos of TX MUX (upper left), RX MUX (right) on top of Robot and horn antenna (lower left).

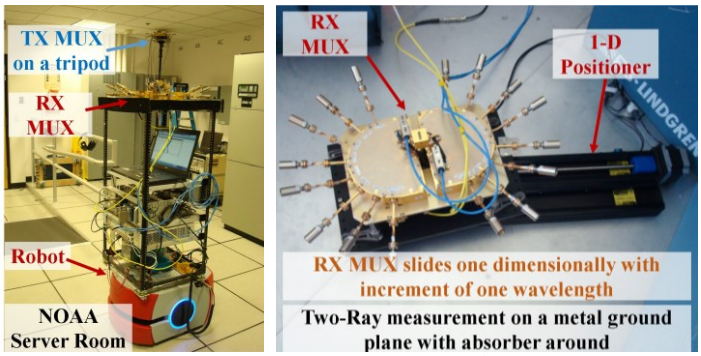

(a) (b)

Fig. 2. Positioning system (a) TX MUX on a tripod and RX MUX on the robotic positioner (for moving cases); (b) RX MUX on a 1-D positioner (for static cases).

3-GHz intermediate frequency (IF) signal with BPSK modulation with a 2047-bit pseudorandom (PN) code word. The bit (or chip) rate is 2 Gbits/s, yielding a delay resolution of 0.5 ns and a maximum delay span of 1023.5 ns. The RF section then up-converts the IF signal to 60.5 GHz. The maximum transmit power for the TX MUX amplifiers is 20 dBm.

The RX MUX has 16 low-noise amplifiers (LNAs) with noise figures < 5 dB. The MUX output is down-converted to 3 GHz, amplified, and then digitized at 40 Gsamples/s. The analog-to-digital converter (ADC) is 8 bit with a programmable IF amplifier. The raw IF data for all 128 channels are then stored on a solid-state drive along with location information from the positioners. The dynamic range of the system for path-loss measurements is 162.2 dB[1]. We synthesized the omni-directional CIR by combining 128 directional CIRs using the SAGE algorithm. The maximum CIR or power delay profile (PDP) updated rate is 488,519 CIRs per second, or 3816 CIRs per second for omni-directional CIRs. The maximum CIR update rate is only available for a short duration until the memory in the digitizer is full.

The MIMO antenna arrays are shown in Fig. 1. The half power beamwidth of the SFHs is 22.5°. The TX multiplexer has 8 antennas which covers 180° in the azimuthal plane (adjacent antennas are 22.5° apart). The RX MUX includes 16 antennas that provide 360° azimuth coverage. Odd antennas have zero elevation angles, while even indices are tilted up (or tilted down depending on test cases) by 22.5° to provide elevation plane coverage. The RX MUX has a second configuration which allows both hemispheres of the antenna arrays to be stacked vertically. In this configuration, the angle between antennas is reduced to 11.25°, and the antennas are replaced with 11.25° beamwidth, 25 dBi gain SFHs. This increases the dynamic range to 169 dB while allowing greater angular resolution.

The MUXs are electronically-switched and controlled by the synchronization and timing circuits. The switching time is less than 25 ns for both TX and RX MUXs. To avoid switch rise-and-fill times, two CIRs (2047 ns) are collected but only one CIR (1023.5 ns) is extracted for channel modeling.

C. *Positioning Systems*

A mobile positioner is used for mobile measurements, and a 1-D positioner is developed for static test cases. Figure 2(a) shows the TX MUX mounted on a tripod at ceiling height to simulate a Wi-Fi deployment in a server room. The RX MUX is mounted on the mobile positioner and is ready to make an automated measurement.

Figure 2(b) is the RX MUX and precision 1-D positioner on a metal ground plane. The TX MUX was also positioned on the ground plane at a fixed point. This configuration was used to measure the two-ray channel. The precision 1-D positioner was used to move the receiver in one-wavelength steps, relative to the transmitter. This allowed local moving averaging to remove small-scale fading, as well as characterization of the reflected signals from the metal ground plane. Results of a two-ray ground bounce response is given in Section IV.B. The 1-D positioner has a minimum step size of 6.35 μm and a range of 30 cm.

III. SYSTEM CALIBRATION

A. *Pre-distortion Filters*

In order to compensate for the non-ideal hardware transfer functions of the transmitter and receiver chains, system calibration is necessary. In previous work related to our 83 GHz system, a post-distortion filter was implemented [3]. Pre-distortion filtering, however, is preferable because it can be applied to high signal-to-noise ratio data at the transmitter. This avoids increasing the noise level at the receiver. The pre-distorted signal is generated by the AWG as well.

Since the amplifiers and waveguides of the TX and RX MUX chains are slightly different, the 128 channels must be equalized individually. Let the measured baseband frequency response of the i^{th} transmitter and j^{th} receiver chain be:

$$Y_{ij}(f) = W_{ij}(f) \cdot P(f) \cdot H_i^{TX}(f) \cdot G_i^{TX}(f) \cdot H_{ij}(f) \cdot G_j^{RX}(f) \cdot H_j^{RX}(f) + N(f), \quad (1)$$

[1] This is determined for the 0.1 dB saturate TX power for the power amplifiers (+20 dBm) + antenna gains (36.2 dB) – RX Noise floor (-78 dBm *ktB* + LNA noise figure 5 dB) + processing gain (33 dB).

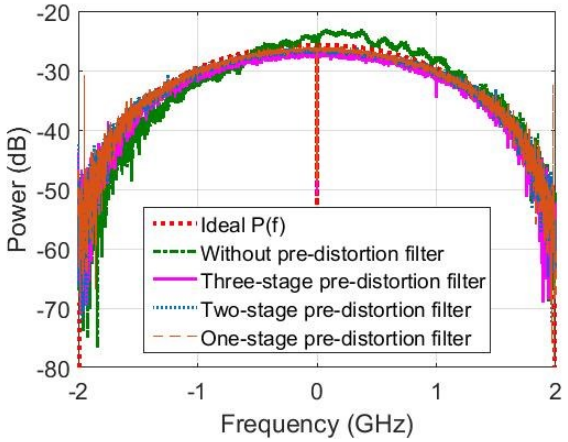

Fig. 3. Power spectrum with and without pre-distortion filter for the 2nd TX antenna and 2nd RX antennas using B2B calibration.

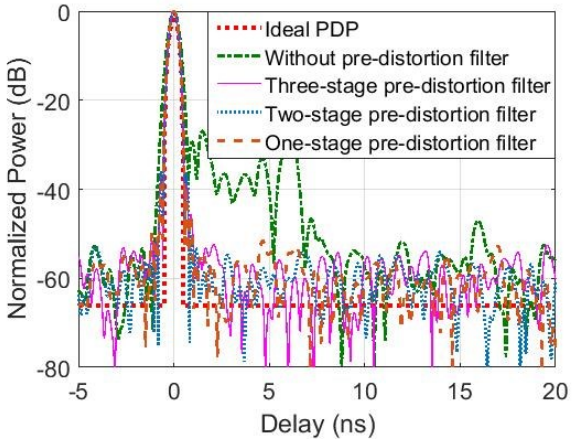

Fig. 4. Example individual normalized power-delay profiles with and without the pre-distortion filter for the 2nd TX antenna and 2nd RX antenna using B2B calibration.

where $W_{ij}(f)$ denotes the pre-distortion filter, $P(f) = p(f) \cdot p^*(f)$ the matched-filter response of the ideal PN sequence $p(f)$, $H_i^{TX}(f)$ and $G_i^{TX}(f)$ the respective transfer function and antenna pattern of the transmitter and $H_j^{RX}(f)$ and $G_j^{RX}(f)$ the same for the receiver, $H_{ij}(f)$ the channel transfer function, and $N(f)$ the system noise. The calibration is based on a back-to-back (B2B) method [6]. In this method, the antennas are removed ($G_i^{TX} = G_j^{RX} = 1$) and the TX and RX connected directly through waveguides and attenuators such that $H_{ij} = A$. The B2B measurement then follows from (1) as:

$$Y_{ij}^{B2B}(f) = \frac{1}{M}\sum_{m=1}^{M} Y_{ij}^{m}(f; G_i^{TX} = G_j^{RX} = 1; H_{ij} = A) \quad (2a)$$

$$\approx W_{ij}(f) \cdot P(f) \cdot H_i^{TX}(f) \cdot A \cdot H_j^{RX}(f). \quad (2b)$$

Averaging in (2a) over M samples indexed through m is carried out to virtually eliminate noise such that the approximation in (2b) holds; we found that M = 128 was sufficient.

The design criteria for the pre-distortion filter is that the output of the B2B measurement be the ideal matched-filter response (plus the attenuators), or

$$Y_{ij}^{B2B}(f) = A \cdot P(f). \quad (3)$$

Now for convenience, (2b) can be rewritten as

$$Y_{ij}^{B2B}(f) \approx W_{ij}(f) \cdot Y_{ij}^{B2B}(f; W_{ij} = 1). \quad (4)$$

By equating (3) and (4), the solution for the pre-distortion filter is given as

$$W_{ij}(f) = \frac{A \cdot P(f)}{Y_{ij}^{B2B}(f; W_{ij} = 1)}. \quad (5)$$

What remains is to take a B2B measurement with no filter $Y_{ij}^{B2B}(f; W_{ij} = 1)$; i.e., with the ideal PN sequence applied at the input.

Fig. 3 displays the power spectrum, $\left|Y_{ij}^{B2B}(f)\right|^2$ both with and without filtering for $i = j = 2$. Notice that the spectrum becomes much smoother with the filter. Also displayed in Fig. 4 is the equivalent power-delay profile $\left|\mathcal{F}^{-1}\left[Y_{ij}^{B2B}(f)\right]\right|^2$ normalized to a peak value of 0 dB. The filter reduces the non-ideal lobes by more than 50 dB from the peak.

Under the assumption of a non-linear system, multiple filter stages can be realized. In each stage, the output of the previous stage is fed to the AWG and the filter is computed recursively as

$$W''_{ij}(f) = \frac{A \cdot P(f)}{Y_{ij}^{B2B}\left(f; W_{ij} = W'_{ij}\right)} \quad (6)$$

.

Also displayed in Figs. 3 and 4 are results up to stage three. Although mild improvement in performance is observed, the system indeed is close to linear and so, to simplify the process, one-stage pre-distortion filters are employed in our system.

To simplify this process further, a calibration matrix approach is used [7]. Through this method, we can reduce the number of measurements from 128 to just 23 by measuring $Y_{ii}^{B2B}(f; W_{ii} = 1), i = 1 \ldots 8$ and $Y_{1j}^{B2B}(f; W_{1j} = 1), j = 2 \ldots 16$. The measurements are applied to compute the filters as

$$W_{ij}(f) = \frac{A \cdot P(f) \cdot Y_{1i}^{B2B}(f; W_{1i} = 1)}{Y_{ii}^{B2B}(f; W_{ii} = 1) \cdot Y_{1j}^{B2B}(f; W_{1j} = 1)}. \quad (7)$$

The calibration matrix method may be particularly useful for Massive-MIMO transfer functions when the number of channels is in the hundreds or thousands. The results were spot-checked by measuring several additional transfer functions. Both measured and calculated transfer functions yielded similar results.

Note that the AWG must generate 128 different waveforms (due to 128 filters) and that the duration of each code word lasts 2047 ns. This requires precision synchronization between the TX and RX to ensure the RX antenna switching is synchronized with the start of a frame of code words. This synchronization is discussed in Section III.C. We also found that the TX MUX needs to warm up to a constant temperature of approximately 35 °C before measurements, because temperature affects the TX power and the pre-distortion filter performance.

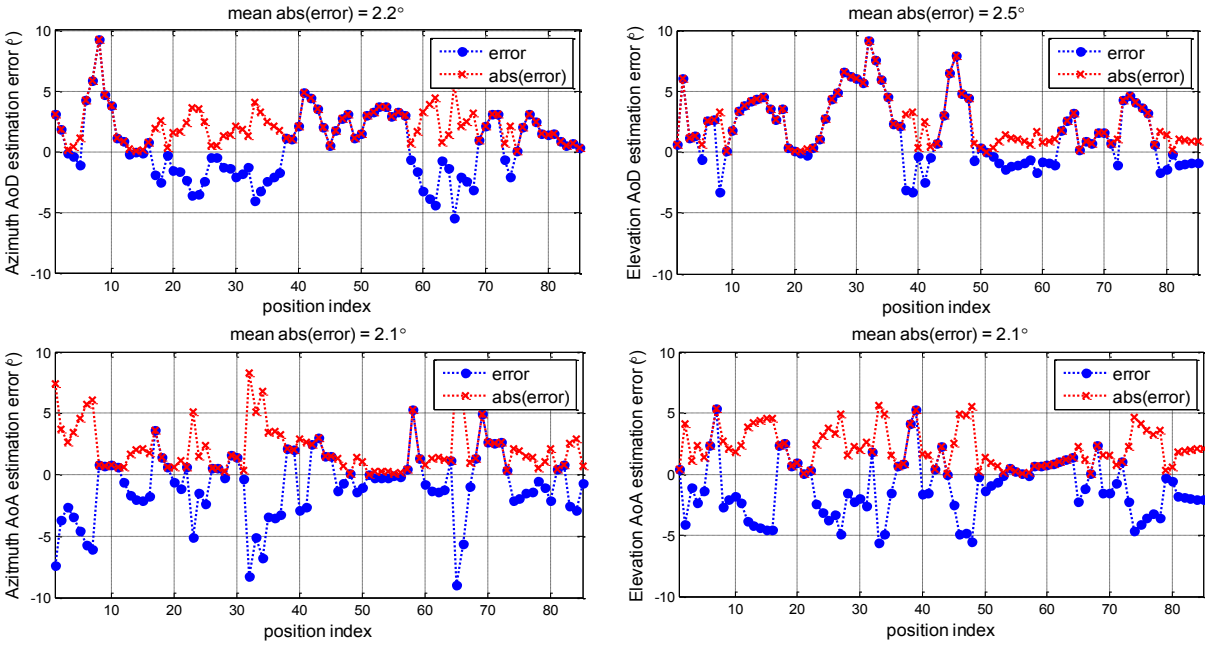

Fig. 5. Error in estimated vs. ground-truth angle. Estimated denotes extracted from measurements while ground-truth denotes reported from navigation system.

The geometries of the TX and RX arrays play an essential role in the precise estimation of AoA and AoD. To accurately measure the array aperture constellation relative to its reference center, a laser interferometer was used as described in [8]. This system has a precision of 50 µm.

B. *Multiplexer Timing Synchronization*

We measured multipath delay using the time lag properties of the PN sequence correlation function. This is a random value without any synchronization between the AWG, RX MUX, TX MUX and digitizer trigger. RX MUX antennas switch once per two code words (2047 ns). This avoids processing code word data during the MUX switching period. The TX multiplexer switches at increments of 32 code words to provide a two code-word window for each of the 16 RX MUX channels. Since the pre-distortion filters make each of the 128 transmitted signals unique, the start times must be aligned between the transmitter code word i=1 and the RX receiver acquisition j=1.

We achieved alignment using a two-stage synchronization approach termed coarse sync and fine sync. The AWG provides start triggers for both TX MUX timing circuitry which uses a 3-bit word to access each of the 8 channels as well as the RX MUX digital switching signal which is a 4-bit word to access each of the 16 channels. This is termed coarse sync, and reduces the random delay to within 2047 ns. However, the AWG itself and the divider/counter module in the RX introduce a random delay between zero and 2047 ns. Hence, we use the pulses from the divider/counter module in the RX to trigger the AWG, and termed fine sync. This removes the random delay between zero and 2047 ns. The coarse sync aligns the indices of code words (but not boundaries) of the TX and RX antenna switching time slots and the fine sync aligns the boundaries (but not indices). Combination of the coarse and fine synchronization provides the required switching synchronization. The synchronization cables can now be removed and timing stability is maintained with rubidium clocks.

The same circuitry, using internal counters, provides a digitizer trigger which is aligned with code word i=j=1, but is repeated at integer numbers of 256 code words. This allows impulses for all channels to be recorded at programmable repetition rates with a granularity of 262 µs and preserve both channel alignment and fine synchronization. The cable length difference and some non-ideal electronic device delays introduce some delay biases. We compensate for these biases by adjusting the start triggers generated by the AWG. Merging Global Positioning System (GPS) into our synchronization circuitries for outdoor measurements is under development. The coarse synchronization is expected to be replaced by the GPS.

IV. System Performance Verification and Initial Results

Initial data from the channel sounder includes AoA and AoD measurements, and a laboratory measurement of a two-ray channel (a direct signal with a ground reflected signal). We also discuss short-term time stability measurements.

A. *AoA and AoD*

The AoA and AoD of the direct multipath component were measured in line-of-sight conditions. The experiments were conducted on a 7 m by 7 m ground plane in a 10 m by 15 m room with cinder block walls [4]. The transmitter was set on a tripod at a height of 2.5 m and the receiver was set on the robotic positioner at a height of 1.5 m. Using the robot's navigation system, we could accurately determine the relative angle (heading) between the TX MUX antenna array and the RX MUX antenna array as well as the velocity of the RX with respect to the TX. The set of experiments consisted of moving the robot in a grid pattern on the ground plane from the fixed transmitter. At each position, the robot collected multiple bursts of data consisting of all 128 antenna channels. We used

the SAGE algorithm to estimate the AoA and AoD on an angular grid with better resolution than our antenna angular separation. The comparison between measured values and the known transmitter/receiver angle for the direct path is given in Fig. 5. We see the SAGE estimations of AoA and AoD have an average error in azimuth less than 2.2° and in elevation less than 2.5°.

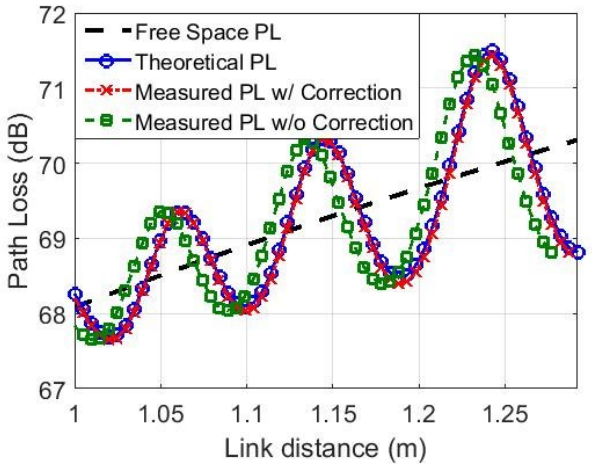

Fig. 6 Two-Ray channel path loss measurement showing good agreement with the theoretical model after applying the phase center correction.

B. Two-Ray Measurements

We collected two-ray data using the precision 1-D positioner with the transmitter and receiver positioned over a conducting ground plane, see Fig. 2(b). The positioner was configured for measurements at one-wavelength spacing for 60 wavelengths. The antennas were vertically oriented and 19.84 cm above the ground plane. By precisely aligning the TX and RX antennas at boresight and adjusting the separation to 1 m, we were able to measure the two-ray lobing pattern of the path loss (PL) caused by the change in the direct and reflected signal path length. This change in path length causes the signals to add constructively or destructively over several phase rotations or cycles, as shown in Fig. 6. Using the geometry of the paths as the 1-D positioner moved and accounting for the antenna patterns, we compared the measured and calculated results. As we can see in Fig. 6, there is an excellent fit. We see the period of the lobing pattern is approximately 0.1 m and its magnitude is 3 dB near 1.25 meters. This increase in lobing magnitude occurred as the reflected path antenna gain increases over link distance due to a decreasing angle relative to the antenna boresight.

We first calculated the antenna separation by measuring the distance between antenna aperture faces, see the green dashed line in Fig. 6. However, the true phase center is inside the horn antenna, which increased the link distance. We obtained the best fit by increasing the measured separation by 1 cm, indicating the location of the phase center of the antennas. By dividing the distance in half, we estimated that the phase center of each antenna is 5 mm behind the antenna aperture. This is useful because it will help in the AoA and AoD estimation with the SAGE algorithm. We have not applied this correction to the AoA and AoD results presented in this paper.

C. Time Stability

The short-term time stability of the CIR is a key characteristic of a channel-sounder measurement which is important for calculation of AoA and AoD. We estimated this by recording 500 CIRs in the B2B configuration. The CIRs were spaced at 2 μs intervals, the period was 1 ms. The data were analyzed by tabulating the phase at the peak of the CIRs. After converting these phase values back to time, we found that the times at the peak were Gaussian distributed with a standard deviation of 8 ps.

V. Conclusion

An untethered 60 GHz MIMO channel sounder has been developed at NIST. The 8×16 MIMO antennas are electronically-switched. The null-to-null bandwidth is 4 GHz, yielding a delay resolution of 0.5 ns. The timing and synchronization enable the employment of a custom pre-distortion for each of the 128 MIMO channels, as well as absolute delay. The sounder has undergone extensive calibration and synchronization. Preliminary measurement results indicate AoA and AoD can be measured with an average error of less than 2.5°. The sounder has been used to measure rack-top-to-rack-top CIRs and inter-rack CIRs with full AoA and AoD capability. These data will be presented in a sequel and could also be used to develop IEEE 802.11ay standards. Future work includes noise analysis and thresholding, developing a positioning system with a new robot and GPS for outdoor environments, detailed analysis of phase stability, and practical characterization of antennas.

References

[1] Federal Communication Commission, Report and Order FCC-16-89, July 14, 2016.

[2] P. B. Papazian, K. A. Remley, C. Gentile and N. Golmie, "Radio channel sounders for modeling mobile communications at 28 GHz, 60 GHz and 83 GHz," *2015 Global Symposium On Millimeter Waves (GSMM),* pp. 1-3, Montreal, QC, 2015.

[3] P. B. Papazian, J. Choi, J. Senic, P. Jeavons, C. Gentile, N. Golmie, R. Sun, D. Novotny, K. A. Remley, "Calibration of millimeter-wave channel sounders for super-resolution multipath component extraction," *2016 10th European Conference on Antennas and Propagation (EuCAP)* , pp. 1-5, Davos, Switzerland, 2016.

[4] P. B. Papazian, C. Gentile, K. A. Remley, J. Senic, N. Golmie, "A Radio Channel Sounder for Mobile Millimeter-Wave Communications: System Implementation and Measurement Assessment," *IEEE Transactions on Microwave Theory and Techniques*, Early View, vol.PP, no.99, pp.1-9, Aug. 2016.

[5] J. A. Fessler and A. O. Hero, "Space-alternating generalized expectation-maximization algorithm," *IEEE Transactions on Signal Processing*, vol. 42, no. 10, pp. 2664-2677, Oct. 1994.

[6] J. A. Wepman, J. R. Hoffman, L. H. Loew, V. S. Lawrence, "Comparison of wideband propagation in the 902-928 and 1850-1990 MHz bands in various microcellular environments," *NTIA Report 93-299*, Sep. 1993.

[7] P. B. Papazian, Y. Lo, J. J. Lemmon, M. J. Gans, "Measurements of Channel Transfer Functions and Capacity Calculations for a 16x16 BLAST Array over a Ground Plane," *NTIA Report TR-03-403*, June 2003.

[8] J. A. Gordon, D. R. Novotny, M. H. Francis, R. C. Wittmann, M. L. Butler, A. E. Curtin, J. R. Guerrieri, "Millimeter-Wave Near-Field Measurements Using Coordinated Robotics," *IEEE Transactions on Antennas and Propagation*, vol. 63, no. 12, pp. 5351-5362, Dec.2015.